The International Journal of Advanced Manufacturing Technology (2022) 123:2575–2591
https://doi.org/10.1007/s00170-022-10341-w

ORIGINAL ARTICLE

In-process belt-image-based material removal rate monitoring for abrasive belt grinding using CatBoost algorithm

Yuxiang Wang[1] · Xiaokang Huang[1] · Xukai Ren[2] · Ze Chai[1] · Xiaoqi Chen[1,3]

Received: 22 May 2022 / Accepted: 17 October 2022 / Published online: 2 November 2022

Abstract

A reliable material removal rate (MRR) prediction method significantly optimizes the grinding surface quality and improves the processing efficiency for robotic abrasive belt grinding. Using worn-belt image features to predict MRR is a direct and reliable method; however, this method is rarely reported at present. This paper proposes an MRR prediction method for Inconel 718 grinding based on the abrasive belt image analysis and categorical boosting (CatBoost) algorithm. During belt grinding, four wear types of abrasive belts, namely fracture, adhesion, rubbing wear, and fall-off, are identified and analyzed. Under various grinding parameters, the experimental MRR rapidly decreases at first, then in a gradual manner. For an effective evaluation of belt wear severity, cutting grain area ratio, color moments, and texture features are extracted from belt images. MRR and abrasive belt image features are strongly correlated after normalization. All image features are taken into account for MRR prediction model training. Verification experiments indicate that the predicted data is in good agreement with the experimental data. The maximum absolute error, mean absolute error, root mean square error, and determination coefficient of the MRR prediction model are 0.17 μm, 0.4 μm, 0.2 μm, and 99.42%, respectively, which are superior to those of other popular machine learning algorithms. In this study, we present a comprehensive understanding of the relationship between MRR and abrasive belt characteristics, as well as demonstrate the feasibility of accurately predicting MRR using the CatBoost algorithm.

Keywords Robotic abrasive belt grinding · Inconel 718 · Material removal rate · Image feature · CatBoost algorithm

1 Introduction

As the final stage of machining, grinding is widely used to process free-form workpieces [1, 2], high-hardness superalloys in the aerospace industry [3], medical instruments[4], etc., and it plays a vital role in obtaining satisfied surface quality of materials [5]. Under the same grinding conditions, abrasive belt grinding commonly yields a higher material removal rate (MRR) and generates less grinding heat than wheel grinding. Therefore, abrasive belt grinding is more efficient than wheel grinding, and the ground materials are less susceptible to surface defects such as burns. To improve the efficiency of the abrasive belt grinding and the quality of the ground surface, automated robotic belt grinding is widely used due to its low cost, good controllability, programmability, and high efficiency [6]. A significant factor affecting the efficiency and quality of grinding is the MRR [7]. Actual MRR, however, is normally unknown due to the complexities of abrasive belt wear mechanisms, the variability of grinding parameters, and the plastic deformation of the contact wheel [8, 9]. Therefore, a suitable method that can accurately evaluate or predict the MRR is of great essence.

There are several factors remarkably affecting the MRR of abrasive belt grinding, including belt speed, grinding force, feed speed, the severity of abrasive belt wear, the curvature of the contact wheel, and the grain size of abrasive

✉ Ze Chai
844707703@sjtu.edu.cn

✉ Xiaoqi Chen
xiaoqichen@swin.edu.au

[1] Shanghai Key Laboratory of Materials Laser Processing and Modification, School of Materials Science and Engineering, Shanghai Jiao Tong University, Shanghai 200240, People's Republic of China

[2] Shaoxing Key Laboratory of Special Equipment Intelligent Testing and Evaluation, Shaoxing 312071, People's Republic of China

[3] School of Engineering, Swinburne University of Technology, Hawthorn, VIC 3122, Australia

belts. A number of studies used these factors to develop mathematical MRR models. Song et al. [10] established a material removal model based on the curvature radius of the convex surface. Ho et al. [11] analyzed the impact of grinding parameters on MRR and optimized the grinding parameters to improve MRR and quantify the impact of these parameters. Li et al. [12] investigated the influences of abrasive size, grinding force, belt speed, and feed speed on the MRR and surface roughness of 45 steel during belt grinding. Li et al. [13] developed an MRR prediction model based on single grain force for robotic belt grinding by studying the abrasive grain distribution and penetration depth. However, these studies did not take into account the wear of abrasive belts when establishing MRR models, which had a significant impact on the model's reliability. In this study, the effect of belt wear on MRR was studied and discussed in detail, and the effect of belt wear was incorporated into the prediction model.

Owing to the complex wear mechanism of abrasive belts, it is difficult to obtain the magnitude of abrasive belt wear from a precise mathematical model [14]. Therefore, most studies used a combination of sensor technology and machine learning techniques to train classification models to identify the wear stages of abrasive belts. By monitoring sensor signals, such as force, vibration, and acoustic emission signals, Pandiyan et al. [15] developed a supported vector machine (SVM) and genetic algorithm-based classification model to distinguish different wear stages of abrasive belts. Chen et al. [16] proposed an acoustic signal-based detection model to detect various periods of belt wear and to determine how much the belt grinding capacity remains, which utilized a random forest classifier as well as a multiple linear regression algorithm. Furthermore, taking advantage of the grinding force, vibration, sound, and acoustic emission signals, Qi et al. [17] established an abrasive belt stage identification model based on improved Mahalanobis distance and convolutional neural networks (CNN). However, they roughly predicted the MRR by merely judging the wear stages of the abrasive belt, ignoring the fact that MRR was not a constant within different wear stages. Instead of dividing the belt wear into different stages, we studied the continuous process of belt wear and proposed a more reliable and accurate MRR prediction model.

Rather than simply classifying the different wear stages of abrasive belts, the monitored sensor information was used directly to predict MRR in some recent studies. In general, abrasive belt grinding monitoring can be divided into two categories: (i) indirect and (ii) direct manners. Currently, most studies use indirect monitoring methods, and studies using direct monitoring methods are rare. The indirect monitoring methods focus mainly on the physical behaviors of belt grinding processes, including sound, vibration, and force, which are affected by different grinding parameters [18, 19]. For instance, Gao et al. [20] proposed an MRR prediction model of robotic belt grinding based on the extreme gradient boosting (XGBoost) algorithm, taking sound signals as input. Wang et al. [21] predicted MRR with the light gradient boosting machine (LightGBM) algorithm by integrating sound signals and grinding spark images, which are essentially indirect monitoring signals. Compared with indirect monitoring methods, direct monitoring focuses on signals that are insensitive to grinding parameters and ambient conditions, such as the features of abrasive belt images. In this paper, utilizing the abrasive belt image features to predict MRR is thus more stable and reliable. In addition, the image features intuitively reflect the severity of the abrasive belt wear and are convenient for acquisition and analysis.

The algorithm used is another key factor affecting the accuracy of MRR prediction. With the development of computer science and technology, various machine learning regression algorithms have been proposed and used in MRR prediction, including SVM [15], CNN [22], XGBoost [20], LightGBM [23], categorical boosting (CatBoost), etc. In the gradient boosting algorithm family, XGBoost, LightGBM, and CatBoost are the most popular and effective algorithms. Compared with XGBoost and LightGBM, CatBoost always has a high accuracy and calculation speed in a large number of competitions and various datasets. In addition, it is an open-source gradient boosting library that leverages categorical features effectively and outperforms existing public gradient boosting implementations based on a set of publicly available datasets [24]. In this paper, we used the CatBoost algorithm to predict MRR, providing more reference data for future studies in related fields.

To address the deficiencies of the existing indirect monitoring methods, this study developed an in-process MRR prediction model for robotic belt grinding of Inconel 718 based on abrasive belt images and the CatBoost algorithm. The rest of the paper is organized as follows. Section 2 introduces the experimental setup and material. Section 3 describes a detailed MRR prediction method involving the abrasive belt image feature extraction and prediction model establishment. The results are presented and discussed in Sect. 4. Finally, several conclusions are drawn in Sect. 5.

2 Experiments

2.1 Experimental setup

In this study, a robotic belt grinding system shown in Fig. 1 was employed to perform belt grinding experiments. The system includes three subsystems, i.e., robot, belt, and monitoring systems. An ATI force sensor is installed at the end of the 6th axis of a robot (IRB6700-200/2.60, ABB) that is controlled by the robot control cabinet. The other

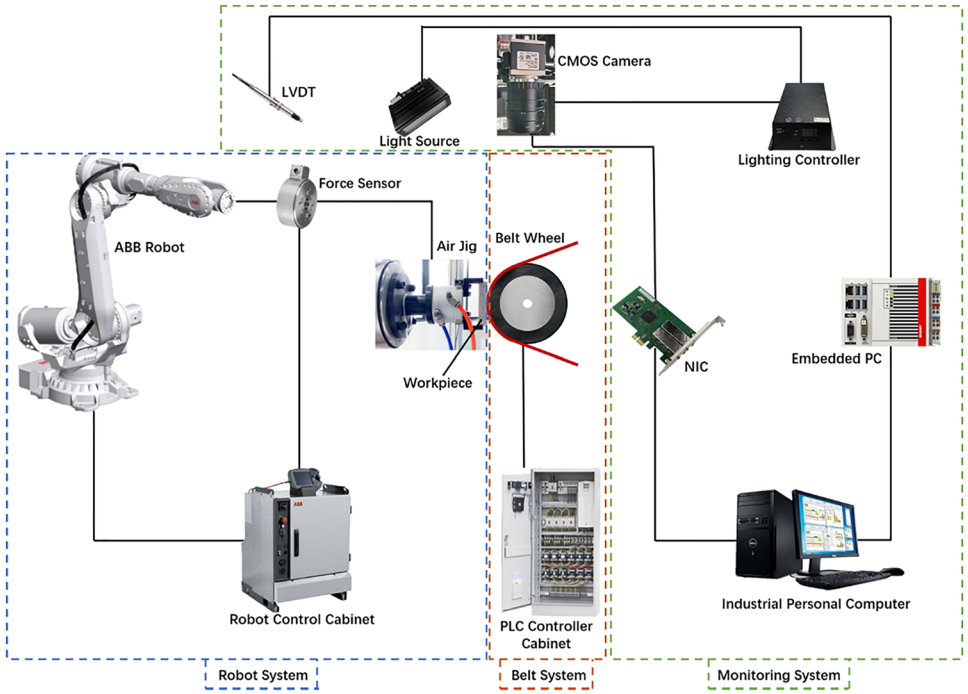

Fig. 1 The robotic belt grinding system used in this study

side of the ATI force sensor connects to an air jig that can clamp the workpiece to be ground. For free-form surface grinding, the constant-force control is realized by using the force sensor.

During the belt grinding process, the abrasive belt was monitored in real time by a complementary metal–oxide–semiconductor (CMOS) camera positioned laterally at a distance of 20 cm from the belt. An auxiliary light source was used to eliminate the interference of ambient light, and the captured belt images were processed on an industrial personal computer with a gigabit ethernet card. With the camera application interface (API), the exposure time was set to 145 ms and the frame rate to 8 fps (detailed technical specifications in Table 1). To obtain the thickness removed by each grinding trial, a linear variable differential transformer (LVDT), which can convert the rectilinear motion of the mechanically coupled workpiece into the electrical signal (a precision of 5 μm), was placed adjacent to the belt wheel. The electrical signal used for removal thickness calculation was then transmitted to the industrial personal computer through an Embedded PC (Beckhoff CX5230).

2.2 Experimental material and process

The chemical compositions of Inconel 718 used in this study are listed in Table 2. The workpiece in this study is an Inconel 718 cuboid piece with a size of 15 mm × 15 mm × 80 mm.

The abrasive belt used in this study is the 15-mm-wide Cubitron 984F with the abrasive grain of 36# produced by the Minnesota Mining and Manufacturing (3 M) Company. The 3 M belt assembled with conical-shaped alumina ceramic grains is very suitable for grinding Inconel 718 with high hardness due to its superior wear resistance and grinding stability. The contact wheel of the belt consists of two parts, i.e., the inner one made of aluminum alloys and the outer one made of rubber. The belt specifications are given in Table 3.

Belt speed, grinding force, and feed speed should all be carefully controlled when belt grinding, as they have a significant impact on grinding efficiency and final product quality. In a trial, the workpiece is ground once from top to bottom.

Figure 2 shows the schematic diagram of a complete grinding trial, which consists of the initial idle stage,

Table 1 Technical specifications of the COMS camera

Camera model	Resolution	Sensor type	Sensor size	Exposure time	Frame rate	Mono/Color	Interface	Exposure control
Basler acA4112-8gc	4096px × 3000px	CMOS	14.1 mm × 10.3 mm	≥ 30 μs	8 fps	Color	GigE	Programmable via the camera API

Table 2 Chemical compositions of Inconel 718

Elements	C	Cr	Ni	Mo	Ti	Nb	Mn	Si	Co	Fe
Content	0.05	18	52.5	2.96	0.9	5.15	0.25	0.22	0.66	Bal

subsequent grinding stage, and final idle stage. Herein, v_b is the belt speed controlled by a programmable logic controller (PLC) cabinet, F is the grinding force between the workpiece and the abrasive belt, and v_w is the feed speed preset in the robotic motion program. In the final idle stage of each trial, the CMOS camera takes 100–120 images to be processed at different belt locations to reduce errors caused by the random distribution of abrasive grains. Besides, at the final idle stage, the thickness change Δd of the ground workpiece is measured at five different locations, and the reported data is the average value of multiple measurements.

The grinding tests were carried out at different belt speeds, grinding forces, and feed speeds, as seen in Table 4. These parameters are well within the range of suitable parameters for fine grinding in actual production. For each experiment, a new abrasive belt was used to ensure an identical initial condition of grinding. The belt grinding would not cease until the Δd at a certain trial was less than the $\Delta d_{\text{first}}/8$ (Δd_{first} was the thickness change obtained at the first trial) because the belt was considered to be failed in this situation. To ensure good repeatability and reliability, all tests were repeated three times. The reported values were the average results of three independent experiments. The standard deviation of MRR lay between 0.11 μm/s and 0.53 μm/s, which was 1–2 orders of magnitude smaller than the values of MRR.

3 Belt-image-based MRR prediction method

3.1 Belt image analysis and feature extraction

RGB images of the abrasive belt contain a great deal of color and texture information that varies with grinding time. The abrasive belt vibrates during belt grinding, and the belt's installation position cannot be guaranteed to be identical for each trial. To obtain regions of interest (ROI) of the same size, the captured belt images must be pre-processed before extracting useful image features. Figure 3a depicts the representative belt image after grinding for 160 s. Filtering, morphological processing, binarization, and custom edge extraction algorithms are used to extract the edge of the abrasive belt, and the result is shown in Fig. 3b. The extracted edge is then fitted with a linear function to obtain a baseline (Fig. 3c) for image cropping. Based on the baselines of the original images, the images are finally cropped to a uniform size (Fig. 3d). After pre-processing, the image feature extraction is performed to obtain the abrasive grain areal ratio (C_r), color moment, and texture information.

Table 3 Specifications of the abrasive belt

Grain (mesh)	Form	Grain	Backing	Coating	Applications
36#	Belt	Zirconia	Finished fabric	Phenolic resin	Heavy grinding

3.1.1 Abrasive grain areal ratio extraction

Figure 4a, b show the processed belt images after grinding for 160 s and 1440 s, respectively. It can be seen from the pre-processed images (Fig. 4a-1, b-1) that red is the primary tone. Extracting the blue channel will effectively remove the red tone information that may obscure other useful features of the image. The processed results are depicted in Fig. 4a-2, b-2. Obviously, there are a large number of bright spots in blue channel images, which are abrasive grain faces mainly induced by abrasive belt wear. Here, two thresholds are set to classify the abrasive grain faces in blue channel images. One depicts the brighter faces in the image, which are caused by the fracture and rubbing wear of grains (Fig. 4a-3, b-3); the other depicts the faces with a weaker brightness, which are primarily caused by rubbing wear of adhesive bond (Fig. 4a-4, b-4). In this study, the abrasive grain areal ratio C_r is defined as:

$$C_r = \lambda_1 \cdot r_1 + \lambda_2 \cdot r_2 \quad (\lambda_1 + \lambda_2 = 1) \tag{1}$$

where r_1 is the areal ratio of brighter grain faces in the ROI; r_2 is the areal ratio of grain faces with weaker brightness in the ROI; and the empirical values of λ_1 and λ_2 are 0.7 and 0.3, considering that the fracture and rubbing wear of grains are dominant in abrasive belt wear.

3.1.2 Color moment extraction

In a digital image, the color is one of the most important attributes that directly reflect what information the image conveys. The color moment is an important aspect of color information, which has proven to be more robust and effective than the traditional histogram-based methods for content-based image retrieval [25]. Compared with the perceptually non-uniform RGB color space, the HSV color space conveys intuitive hue, saturation, and brightness of an image, which are of great importance for distinguishing the differences between abrasive belt images. Figure 5 shows different

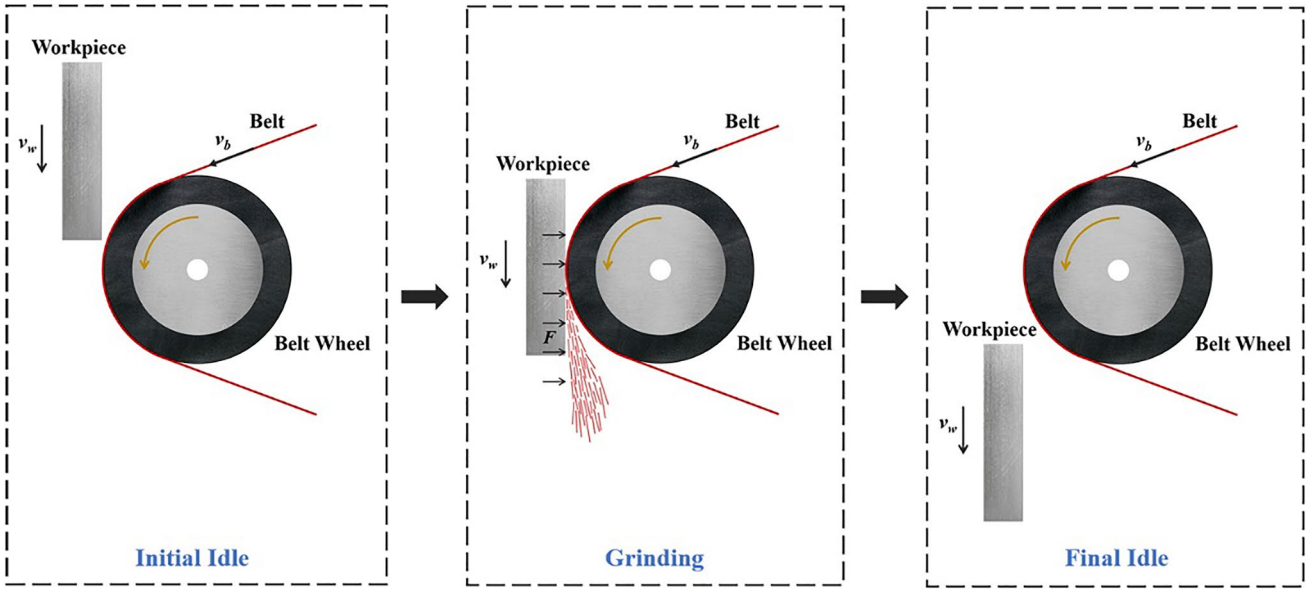

Fig. 2 Schematic diagram of a complete grinding trial

components of color features of the abrasive belt in the HSV color space converted from the RGB color space.

According to Singh et al. [25], the calculation formulas for converting the RGB color space into the HSV color space are expressed as:

$$H = \cos^{-1}\frac{\frac{1}{2}[(R-G)+(R+B)]}{\sqrt{(R-G)^2+(R-B)(G-B)}} \tag{2}$$

$$S = 1 - \frac{3[min(R,G,B)]}{R+G+B} \tag{3}$$

$$V = \frac{R+G+B}{3} \tag{4}$$

where H, S, and V represent the hue channel, saturation channel, and value (also brightness) channel, respectively; R, G, and B represent the red channel, green channel, and blue channel, respectively. In general, the first three color moments of an image, namely mean, standard deviation, and skewness, are most commonly used due to their good stability. The calculation formulas are listed in Table 5.

In Table 5, N is the number of pixels in an image, and p_{ij} is the value of the jth pixel of an image at the ith color channel. Here, we choose the standard deviation of the hue channel (H_std), the value channel (V_std), and the mean and skewness of the saturation channel (represented by S_mean, and S_skew, respectively) as useful features for the abrasive belt wear assessment.

Table 4 Different belt grinding parameters of experiments

Experiment no	Belt speed v_b (m/s)	Grinding force F (N)	Feed speed v_w (mm/s)	Grinding time (s)	Number of trials
1	4.58	40	5	32	60
2	5.49	30	5	32	45
3	5.49	40	5	32	59
4	5.49	40	8	30	48
5	5.49	50	5	32	55
6	6.41	40	5	32	40
7	5.49	40	2	40	36
8	7.33	40	5	32	45

3.1.3 Texture extraction

The image texture analysis plays a key role in many areas including remote sensing [26], medical images [27], and auto driving [28]. The texture is defined as an attribute that describes how gray levels of pixels are arranged in a particular region of a digital image [29]. An effective and widely used method for analyzing image textures is the gray-level co-occurrence matrix (GLCM) analysis [30]. The GLCM provides detailed information on the gray direction, interval, change range, and speed of an image, but cannot describe the texture directly. To quantitatively describe the texture, the relevant statistical attributes based on GLCM need to be extracted. The calculation formulas of statistical attributes are summarized in Table 6.

In Table 6, the GLCM $p_d[i,j]$ is defined by first specifying a displacement vector $d=(dx, dy)$ and counting all pairs of pixels separated by d having gray levels i and j. In this study, vector d is defined as (1,1). The dimension of p_d is

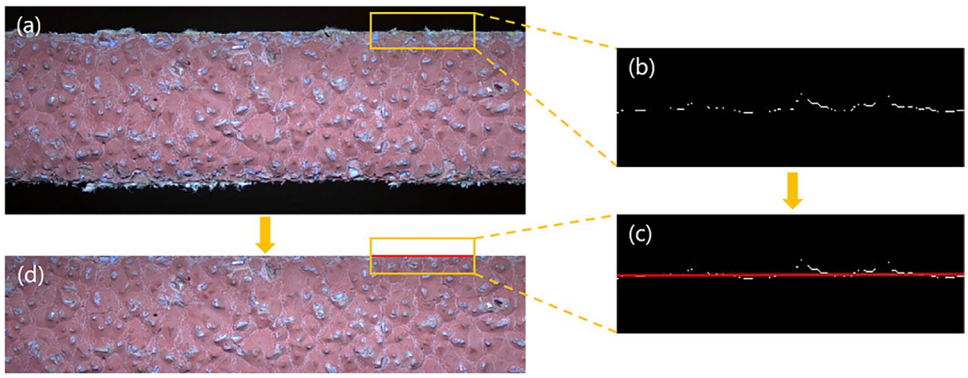

Fig. 3 **a** Representative belt image, **b** part of the extracted edge, **c** part of the baseline, and **d** image of a uniform size

$M \times N$ (16 × 16), representing the number of gray levels in the image. In addition, $P_d\,[i, j]$ with a value of 0–1 is calculated by:

$$P_d[i,j] = \frac{P_d[i,j]}{\sum_{i=0}^{M-1}\sum_{j=0}^{N-1} P_d[i,d]} \tag{5}$$

After normalization, the co-occurrence values of images with different sizes will remain on the same scale.

3.2 MRR prediction model

In order to accurately predict MRR, a model that incorporates all the abrasive belt-feature parameters mentioned above should be developed. A multi-parameter mathematical model is, however, difficult to establish due to the complex influence of multiple sets of abrasive belt feature parameters on the MRR. Fortunately, the CatBoost algorithm is an effective and feasible solution to address such a complex multi-parameter nonlinear problem. The flow chart for establishing the CatBoost algorithm-based MRR prediction model is shown in Fig. 6. The MRR and extracted image features were normalized in this study. The normalization formula is given as:

$$x_n = \frac{x - x_{\min}}{x_{\max} - x_{\min}} \tag{6}$$

where xn is the normalized experimental data, x is the experimental data, $x_{\max}$ is the maximum experimental data, and $x_{\min}$ represents the minimum experimental data. Therefore, the MRR prediction model is fed the normalized Cr, normalized color moments, and normalized texture features, and the output is the model-predicted MRR.

3.2.1 CatBoost algorithm

Figure 7 depicts the structure of the CatBoost algorithm for MRR prediction model establishment. The strength of CatBoost lies in two noteworthy algorithmic advances: (i) application of ordered boosting and (ii) a method for dealing with categorical features [31]. CatBoost uses ordered boosting along with ordered target statistics that are based on the ordering principle to eliminate target leakage and prediction shift problems caused by differences in the distribution of

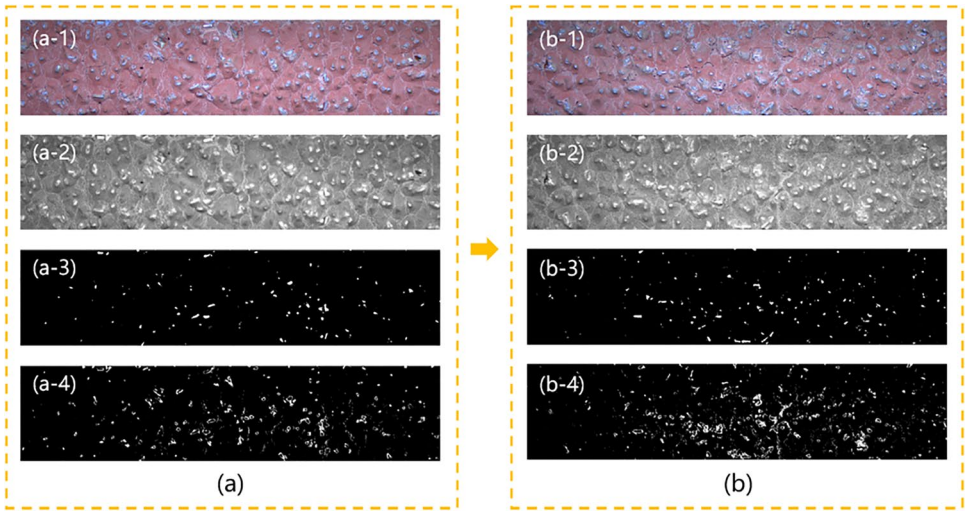

Fig. 4 Image processing of the images after grinding for **a** 160 s and **b** 1440 s, including cropped images (a-1, b-1), images of the blue channel (a-2, b-2), and extracted bright spots (a-3, b-3, a-4, b-4)

Table 5 Color moment calculation formulas of abrasive belts

Features	Calculation formulas
Mean	$E_i = \sum_{j=1}^{N}\left(\frac{1}{N}p_{ij}\right)$
Standard deviation	$\sigma_i = \sqrt{\frac{1}{N}\sum_{j=1}^{N}\left(p_{ij}-E_i\right)^2}$
Skewness	$s_i = \sqrt[3]{\frac{1}{N}\sum_{j=1}^{N}\left(p_{ij}-E_i\right)^3}$

train and test datasets. In addition, one-hot encoding is used for features with fewer categories, and the maximum number of categories for one-hot encoding is controlled by using the one_hot_max_size parameter.

3.2.2 Model training

As introduced in Sect. 2.2, eight experiments with different grinding parameters were performed to obtain the MRR and the abrasive belt images used for image feature extraction. The model was trained based on the CatBoost algorithm using the data of experiment no. 1–6, and prediction accuracy was determined using the data of experiment no. 7–8. The inputs consisted of ten different normalized parameters that described abrasive belt images from various perspectives, and the output was the model-predicted MRR.

In order to determine the optimal hyperparameters of the established MRR prediction model, grid search was employed as a tuning technique. The determination coefficient (R^2) is shown in Fig. 8 as a function of n_estimator and learning_rate. The top R^2 is acquired when the n_estimator is 196, and the learning_rate is 0.07. In this way, depth and max_leaves are also determined, and these hyperparameters are listed in Table 7.

4 Results and discussion

4.1 Experimental MRR and abrasive belt wear

In order to understand the trend of MRR over time under different grinding parameters, experimental MRRs are presented. Furthermore, the abrasive belt morphology at various grinding stages is observed and analyzed by using a scanning electron microscope (SEM, TESCAN, MIRA3).

4.1.1 Experimental MRR

Figure 9 depicts the change of the MRR over time at different grinding parameters, and the MRR data correspond to experiment no. 1–6 in Table 4. The thickness evaluation method, which measures the thickness change of the workpiece over time, is used for the MRR calculation in this study. This method directly reflects the grinding ability of abrasive belts in real time. The MRR is calculated by:

$$\mathrm{MRR} = \frac{\Delta d}{\Delta t} \tag{7}$$

where Δd is the thickness change of the workpiece and Δt is the duration time. It is reasonable that the MRR gradually decreases with prolonging the grinding time, as seen in Fig. 9. At the same belt speed and feed speed, the MRR curves corresponding to the grinding forces 50 N, 40 N, and 30 N are located in the uppermost, middle, and lowermost parts of the figure, respectively, implying that the grinding force has a dramatic impact on MRR. Moreover, MRR increases as the belt speed increases when the grinding force and feed rate remain constant. Nevertheless, it is difficult to determine whether MRR is dependent on feed speed, possibly because feed speed has a smaller impact on MRR than belt speed and grinding force.

The grinding parameter and grinding time-dependent MRR can be understood from the model proposed by Hammann et al. [32].

$$\mathrm{MRR} = C_A \cdot k_A \cdot k_t \cdot \frac{F_n v_b}{v_w L_w} \tag{8}$$

where C_A is the grinding process constant; k_A is the resistance factor between the belt and the workpiece; k_t is a variable quantity and can evaluate the wear of the abrasive belts; L_w is the contact width; and F_n, v_b, and v_w are the grinding force, belt speed, and feed speed, respectively. Figure 9

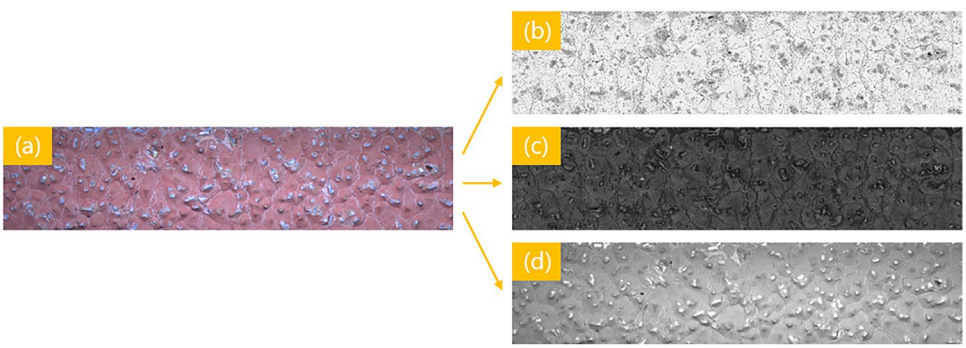

Fig. 5 **a** Cropped RGB image of the abrasive belt, **b** hue channel image, **c** saturation channel image, and **d** value channel image

Table 6 Texture feature calculation formulas of the abrasive belt

Features	Calculation formulas	Application
Angular second moment	$\mathrm{ASM} = \sum_{i=0}^{M-1} \sum_{j=0}^{N-1} P_d[i,j]^2$	Measurement of uniformity of gray distribution
Entropy	$\mathrm{Ent} = \sum_{i=0}^{M-1} \sum_{j=0}^{N-1} P_d[i,j] ln P_d[i,j]$	Measurement of information content
Contrast	$\mathrm{Con} = \sum_{i=0}^{M-1} \sum_{j=0}^{N-1} (i-j)^2 P_d[i,j]$	Measurement of local variations
Correlation	$\mathrm{Cor} = \frac{\sum_{i=0}^{M-1} \sum_{j=0}^{N-1} [ijP_d[i,j]] - \mu_i \mu_j}{\sigma_i \sigma_j}$ $\mu_i = \sum iP_d[i,j]$ $\sigma_i^2 = \sum i^2 P_d[i,j] - \mu_i^2$	Measurement of image linearity
Homogeneity	$\mathrm{Hom} = \sum_{i=0}^{M-1} \sum_{j=0}^{N-1} \frac{P_d[i,j]}{1+\lvert i-j \rvert}$	Measurement of local change of the texture

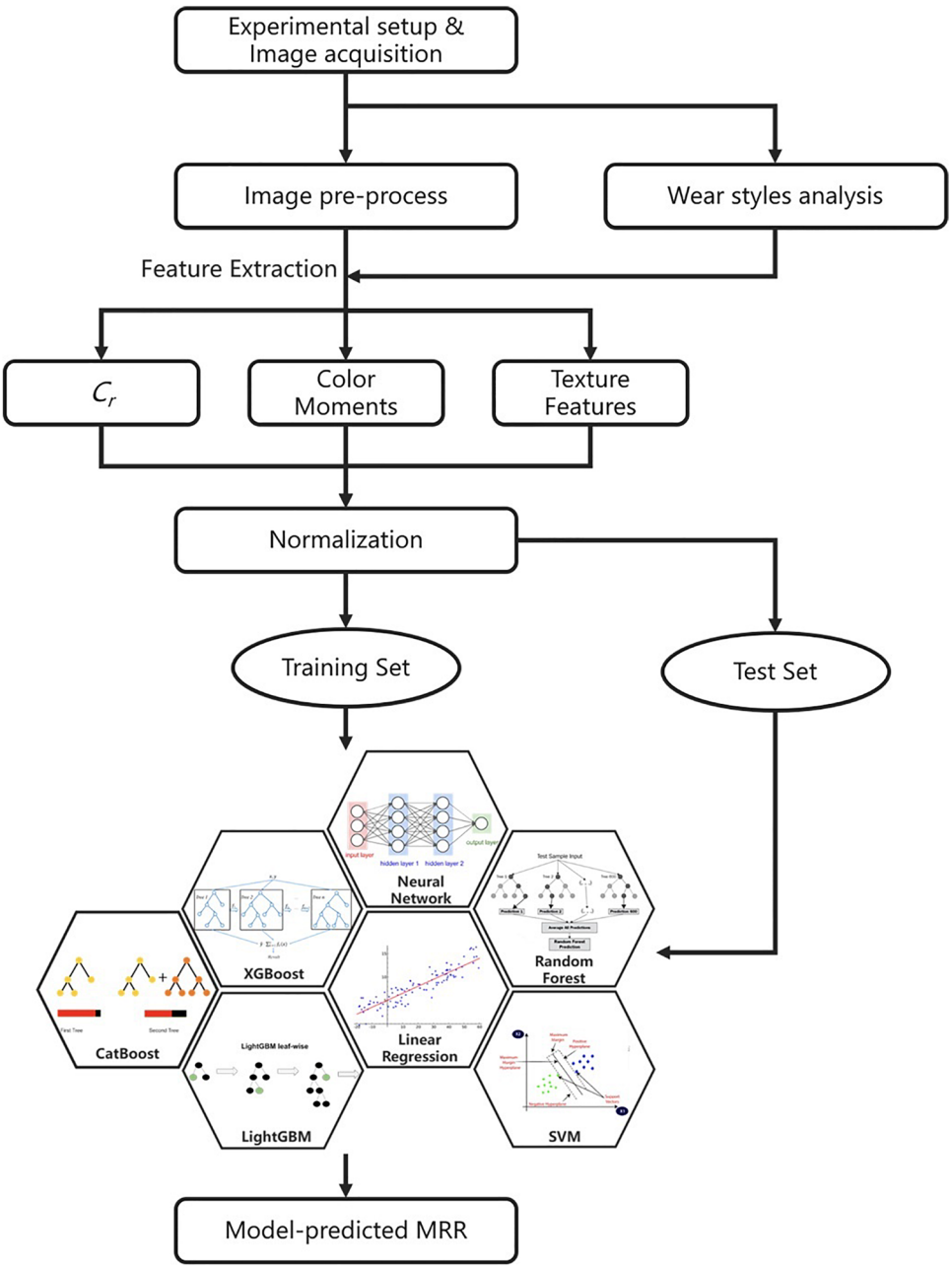

Fig. 6 The framework of MRR prediction model establishment

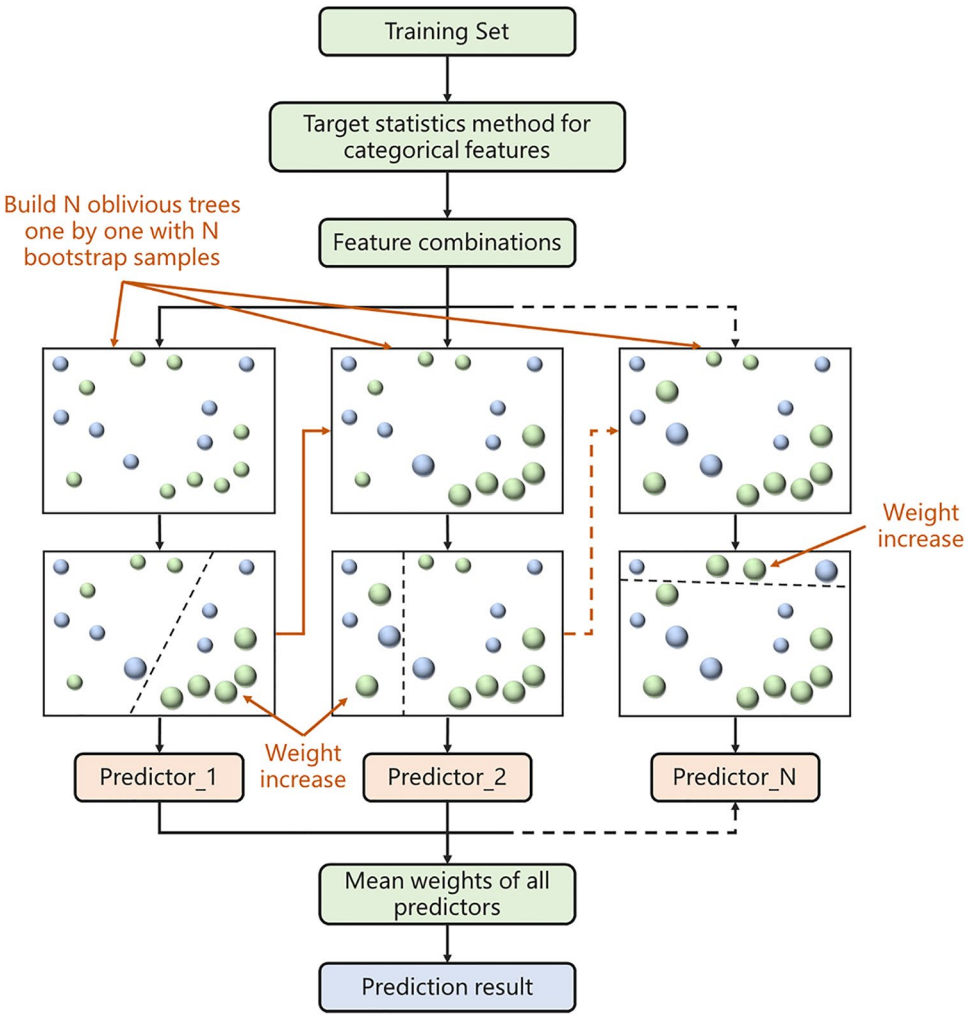

Fig. 7 Structure of the CatBoost algorithm

clearly illustrates the relationship between MRR and grinding parameters in Eq. 8. In view of the fact that C_A, k_A, L_w, F_n, v_b, and v_w are constant during abrasive belt grinding, the change of the quantity k_t leads to the decrease of the MRR. Thus, realizing the MRR prediction relies mainly on the accurate evaluation of the abrasive belt wear.

Figure 10 shows the thickness change Δd of the workpiece before and after each grinding cycle at five different

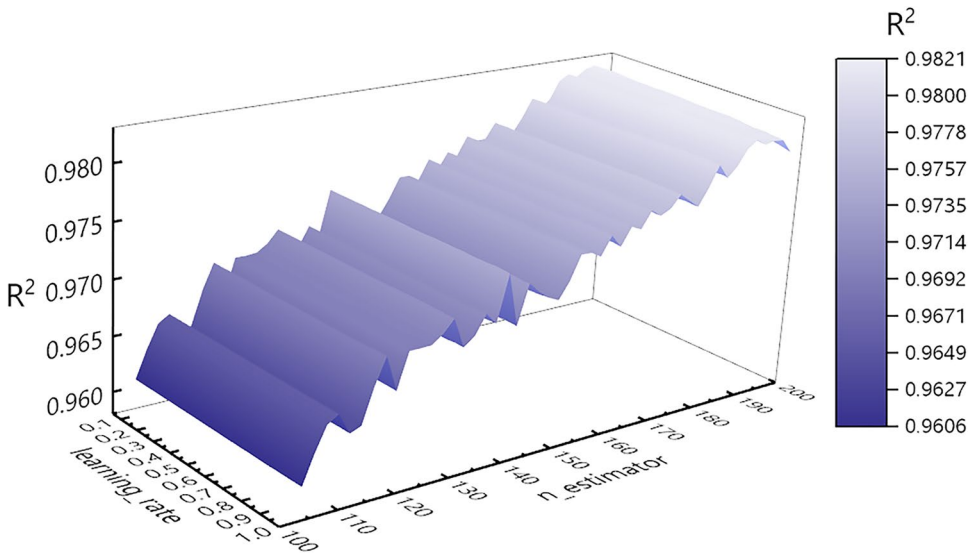

Fig. 8 Determination coefficient (R^2) as a function of n_estimator and learning_rate

Table 7 Part of hyperparameters of CatBoost

Hyperparameters	Value
n_estimator (iterations)	196
learning_rate	0.07
Depth	6
max_leaves	64

locations 1, 2, 3, 4, and 5, and the grinding parameters are 5.49 m/s belt speed, 50 N grinding force, and 5 mm/s feed speed. The sample actually has a flat ground surface with a standard deviation of less than 6 μm for Δd determination.

In this study, the surface roughness of ground samples was less than 3.5 μm. The surface roughness was measured by a roughness tester (SJ-410, Mitutoyo, Kawasaki, Japan) and the measuring direction was perpendicular to the grinding direction.

4.1.2 Abrasive belt wear behavior

According to SEM images in Fig. 11a–f, four belt wear types can be observed, namely fracture, adhesion, rubbing wear, and fall-off. Owing to the excessive tangential forces during belt grinding, abrasive grains tend to break off in the middle, leaving a smooth, flat fracture surface that may be lower than the adhesive bond around abrasive grains (Fig. 11b). During belt grinding, adhesion occurs when the workpiece material adheres to abrasive grains. The adhesion layer was examined by an energy-dispersive X-ray spectrometer (EDS, Oxford, Aztec, X-MaxN8), as seen in Fig. 11c. The major elements of Inconel 718 (Ni, Fe, and Cr) were detected at point P. Moreover, rubbing wear (Fig. 11e) is a very common occurrence in belt grinding, including grain rubbing wear and adhesive bond rubbing wear. Fall-off occurs when

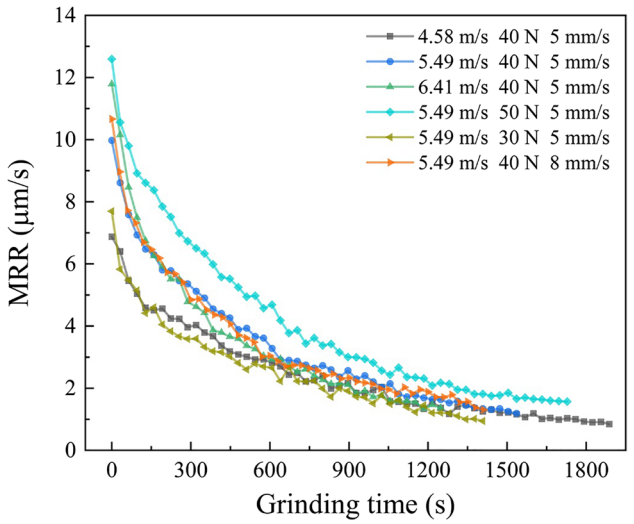

Fig. 9 MRR as a function of grinding time under different grinding parameters

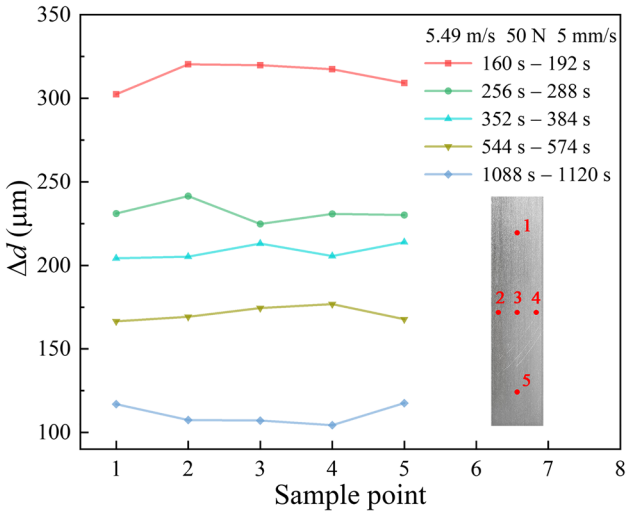

Fig. 10 Thickness change of the workpiece before and after each grinding cycle at 5 different locations

abrasive grains completely fall off the abrasive belt, leaving a pit behind, as seen in Fig. 11f.

During belt grinding, the abrasive belt morphology changes significantly. Figure 12a–d show the abrasive belt images captured before and after belt grinding for 160 s, 600 s, and 1440 s. Specifically, The labels (1)–(4) in Fig. 12 represent fracture, adhesion, rubbing wear, and fall-off of abrasive belts, respectively. A few grain fractures can be observed on the brand-new abrasive belt (Fig. 12a). As abrasive belts are always folded tightly during transport, the abrasive grains rub against each other and eventually fracture. In the initial period of belt grinding, the high-protrusion abrasive grains first contact the workpiece and remove the material as discontinuous chips under the effect of plowing, leading to a very high MRR. However, the MRR decreases dramatically (the initial stage of curves in Fig. 9) because these protruding abrasive grains with strong penetration ability withstand the excessive tangential force, leading to a large number of fractures. After fracture, the abrasive grain edges remain sharp and maintain a moderate grinding ability. After the dramatic decrease, the MRR should have increased or remained constant due to the growing number of lower protruding abrasive grains and the newly re-sharpened abrasive grains resulting from the fracture. However, the MRR smoothly declines in Fig. 9. This is because other types of grain wear are gradually dominant, as seen in Fig. 12b–d. Since a great deal of heat is generated during belt grinding, the temperature of the workpiece surface increases rapidly, and the hardness of the workpiece decreases as a consequence [33]. Therefore, the workpiece debris easily adheres to abrasive grains and covers the abrasive grain edges, thereby reducing the grinding performance of these abrasive grains. Additionally, due

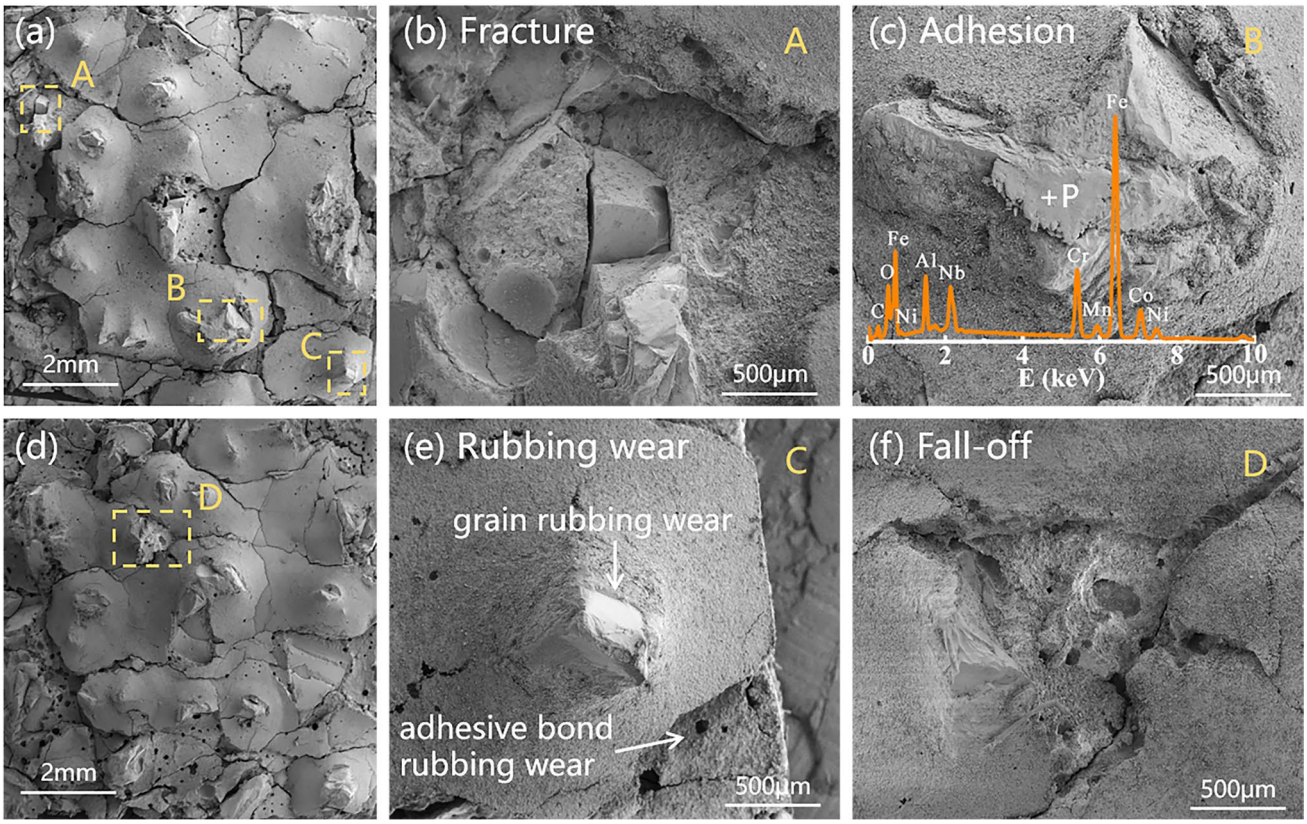

Fig. 11 SEM images of different belt wear styles

to the grain rubbing wear, the material is barely removed when these blunt abrasive grains slide across the surface. It is the rubbing wear of the adhesive bond that causes the low adhesion strength of the resin bond. Besides, some of the abrasive grains, whose tips are lower than the surrounding adhesive bond after the fracture, are useless for grinding. Consequently, MRR shows a slight and smooth decline after the rapid decrease in the initial period, which is in line with the curves in Fig. 9.

4.2 Relationship between belt image features and MRR

C_r as a function of grinding time under different grinding parameters is presented in Fig. 13. The C_r shows an opposite trend to the MRR, indicating that the C_r is positively correlated with the abrasive belt wear.

Figure 14 depicts four color moments as functions of grinding time in experiment no. 1–6. It can be seen from Fig. 14a–d that the H_std and S_mean are negatively related to the abrasive belt wear, while the S_skew and V_std display the opposite trend.

Figure 15 shows the features extracted from the image texture as functions of grinding time in experiment no.1–6. As seen from Fig. 15, the Ent and Con are negatively related to the abrasive belt wear, while it is opposite for the ASM, Cor, and Hom.

As can be seen from Figs. 9, 13, 14 and 15, both the MRR and extracted image features change monotonically with grinding time, showing a similar trend under different grinding parameters. The MRR and the extracted image features are on the same scale after normalization.

Three scatter diagrams (Fig. 16a–c) are constructed using normalized feature parameters as abscissas and normalized MRRs as ordinates in order to illustrate the correlation between normalized MRRs and extracted image features. The abrasive grain areal ratio is C_r, and the color moments and texture features are represented by H_std and Hom. Each figure contains all data from experiment no.1–6. It can be seen from Fig. 16 that the normalized H_std and Hom positively correlate with the normalized MRR, whereas the normalized C_r negatively correlates with the normalized MRR. Specifically, as the normalized C_r approaches 1, the experimental MRR is close to 0, indicating failure of the abrasive belt (Fig. 16a). Meanwhile, the dependence of normalized MRR on normalized H_std or Hom is almost linear, although some data of the Hom somewhat diverge (Fig. 16b, c).

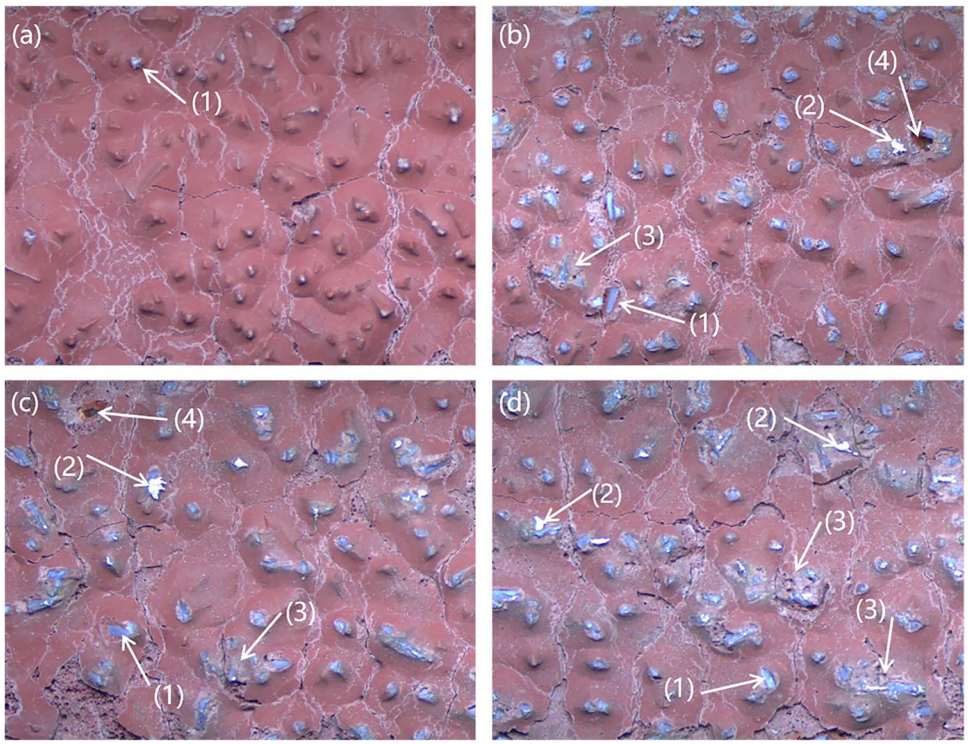

Fig. 12 Abrasive belt images after grinding for **a** 0 s, **b** 160 s, **c** 600 s, and **d** 1440 s. The labels (1), (2), (3), and (4) represent fracture, adhesion, rubbing wear, and fall-off of abrasive belts, respectively

4.3 MRR prediction

4.3.1 Accuracy assessment

To assess the accuracy of the MRR prediction, four classic performance indices have been employed, and the relevant calculation formulas are depicted in Table 8.

In Table 8, n is the data size; y_i and x_i are the predicted and true values of the ith sample. To assess the magnitude of deviation between the predicted and experimental MRR, the indices maximum absolute error (MaAE), mean absolute error (MAE), and root mean square error (RMSE) are used. The R^2 refers to how well the regression model fits the experimental data. In this study, the MaAE, MAE, RMSE, and R^2 of the CatBoost algorithm-based MRR prediction model were 0.17 μm, 0.4 μm, 0.2 μm, and 99.42%, respectively. Figure 17 compares the experimental MRR data of experiment no.7–8 and denormalized model-predicted data. The denormalized model-predicted MRR is calculated by:

$$\mathrm{MRR}_d = \mathrm{MRR}_t + \mathrm{MRR}_p \cdot \left(\mathrm{MRR}_i - \mathrm{MRR}_t\right) \tag{9}$$

where MRR_d is the denormalized model-predicted MRR; the MRR_t is the MRR acquired when the grinding terminates; the MRR_p is the predicted MRR from the prediction model; and the MRR_i is the MRR acquired from the initial experimental trial. In these two sets of verification experiments, the deviation between the model-predicted and experimental values lay between 0.05 and 0.39 μm/s, which were 1–2 orders of magnitude smaller than the values of MRR. It can be seen from Fig. 17 that the model-predicted data and the experimental data for experiment no. 7–8 are in good agreement. The reliability of the prediction model can be determined by this result.

Thus, if the initial and terminated MRR as well as images of a brand-new abrasive belt and a failed abrasive

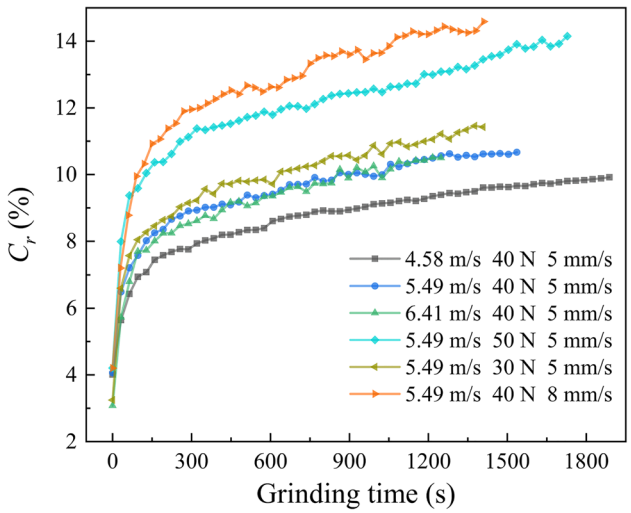

Fig. 13 C_r as a function of time under different grinding parameters

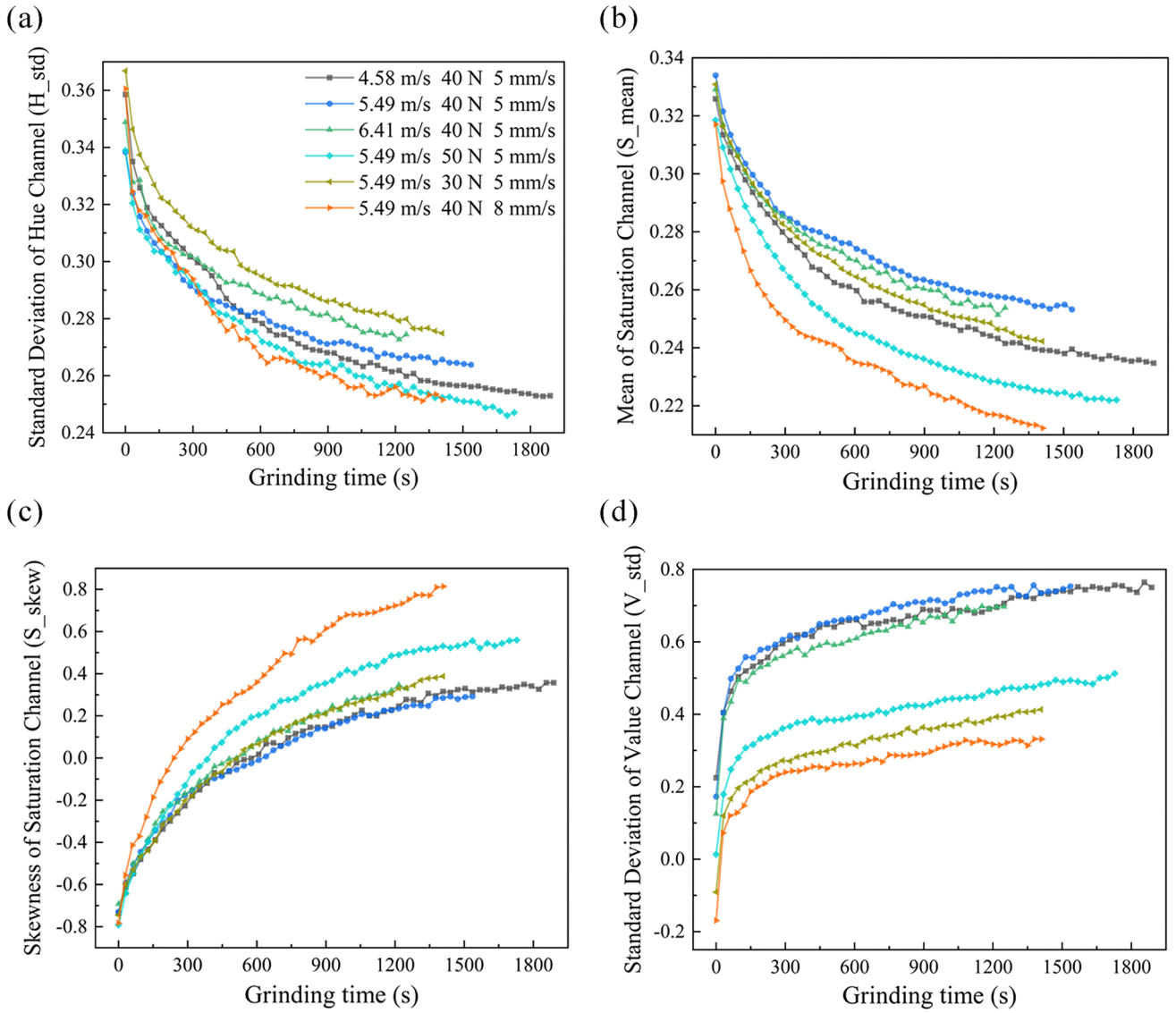

Fig. 14 **a** H_std, **b** S_mean, **c** S_skew, and **d** V_std as functions of time under different grinding parameters

belt are acquired in actual use, then the MRR of the brand-new abrasive belt in the grinding process can be predicted based on the MRR prediction model and Eq. 9. Specifically, the initial MRR and the images of a brand-new abrasive belt can be directly acquired at the first grinding trial under given grinding parameters, and the terminated MRR and the corresponding images can be obtained by grinding a failed abrasive belt. The terminated MRR and the images are valid and acceptable as long as the MRR acquired by a certain grinding trial is slightly less than one-eighth of that obtained by the first grinding trial. Otherwise, the grinding process will continue until the MRR meets the requirements. The main disadvantage of this model is that the necessary condition for the model to be able to predict is that the initial and terminated MRR and abrasive belt images need to be obtained in advance. Therefore, the follow-up work is to build a grinding database, which stores the initial and terminated MRR and abrasive belt images under different grinding parameters and abrasive belt parameters.

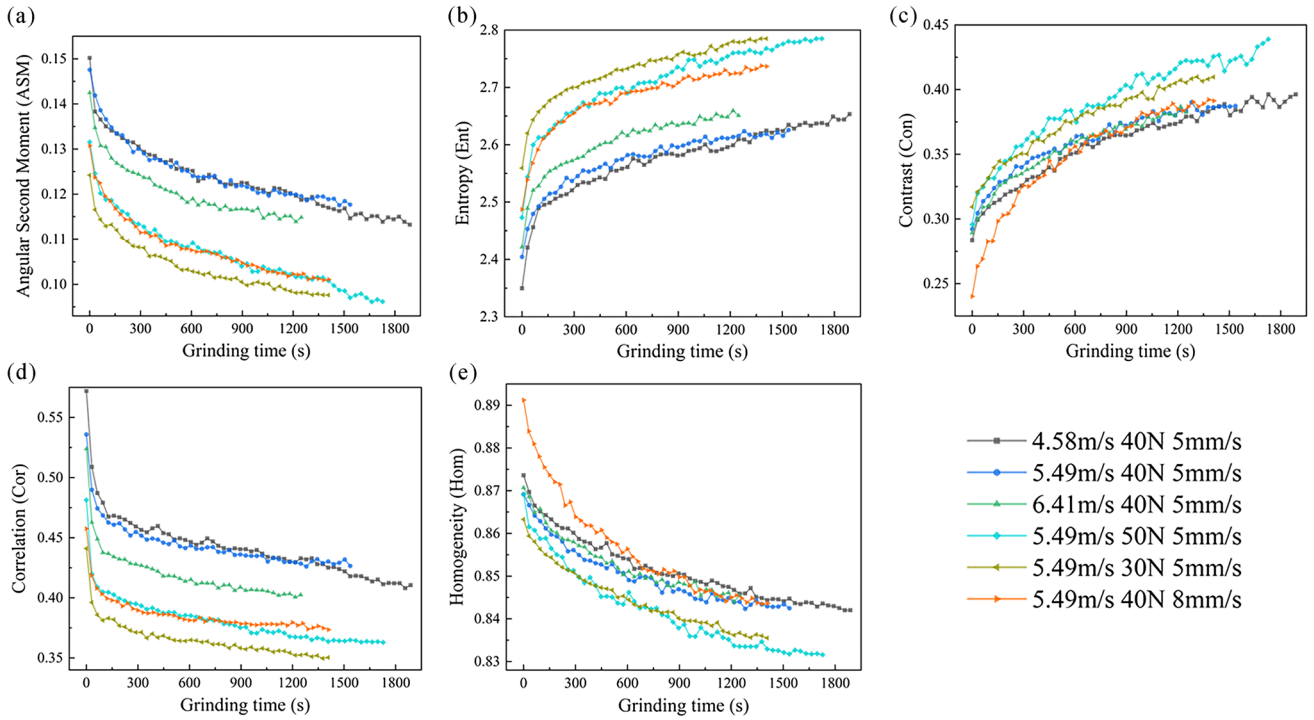

Fig. 15 **a** ASM, **b** Ent, **c** Con, **d** Cor, and **e** Hom as functions of time under different grinding parameters

4.3.2 Comparison of different algorithms

To demonstrate the superiority of the CatBoost algorithm we used, most mainstream machine learning algorithms, including XGBoost, LightGBM, LinearRegression, SVM, Neural Network, and Random Forest, were used to train the MRR prediction model for comparison. Their training datasets and test datasets were identical to those used in the CatBoost algorithm. The gray histogram in Fig. 18 shows the R^2 of these machining learning algorithms, and the CatBoost provides the best fit to the experimental data. According to the rest of the histograms in Fig. 18, the CatBoost algorithm has the lowest MaAE, MAE, and RMSE values. Thus, the CatBoost algorithm exhibits a higher predictive reliability and a lower error rate than other algorithms.

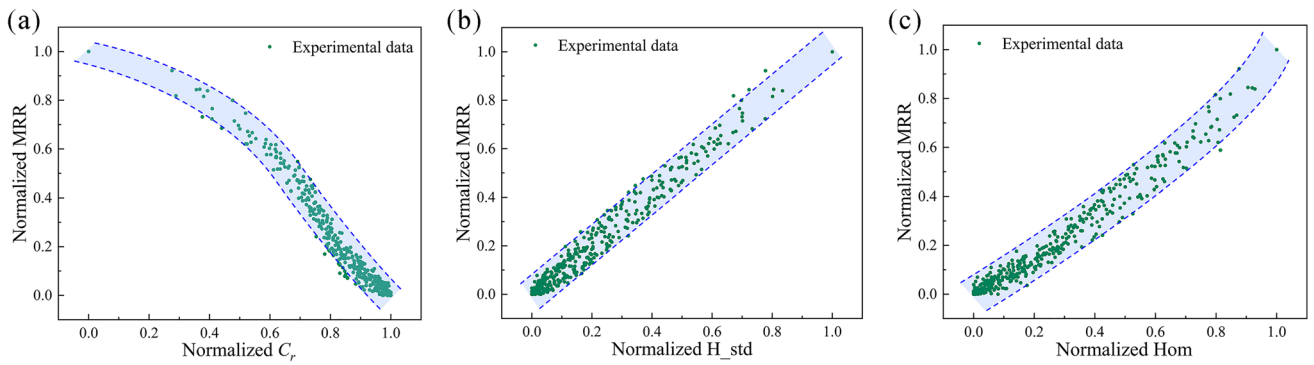

Fig. 16 Relationship between normalized MRR and **a** normalized C_r, **b** normalized H_std, and **c** normalized Hom

Table 8 Calculation formulas of performance indices

Performance indices	Calculation formula
Maximum absolute error (MaAE)	$\mathrm{MaAE} = max\{\lvert y_i - x_i \rvert\}$
Mean absolute error (MAE)	$\mathrm{MAE} = \frac{\sum_{i=1}^{n} \lvert y_i - x_i \rvert}{n}$
Root mean square error (RMSE)	$\mathrm{RMSE} = \sqrt{\frac{\sum_{i=1}^{n} (y_i - x_i)^2}{n}}$
Coefficient of determination (R^2)	$R^2 = 1 \frac{\sum_{i=1}^{n} (y_i - x_i)^2}{\sum_{i=1}^{n} (y_i - \bar{y})^2}$ $\bar{y} = \frac{\sum_{i=1}^{n} y_i}{n}$

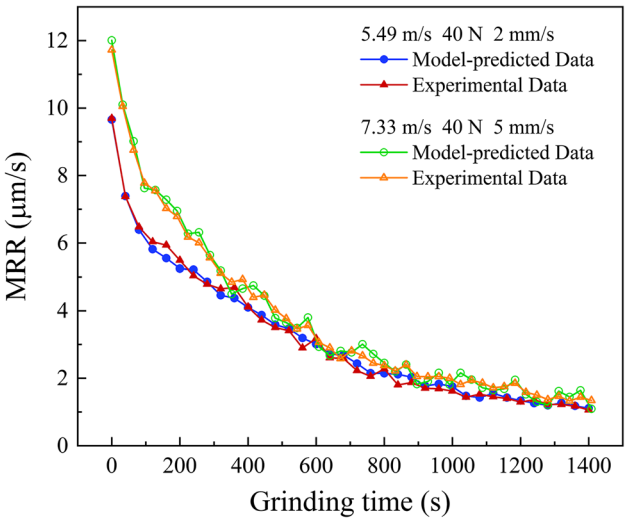

Fig. 17 Comparison of the experimental and predicted MRR data for experiment no.7–8

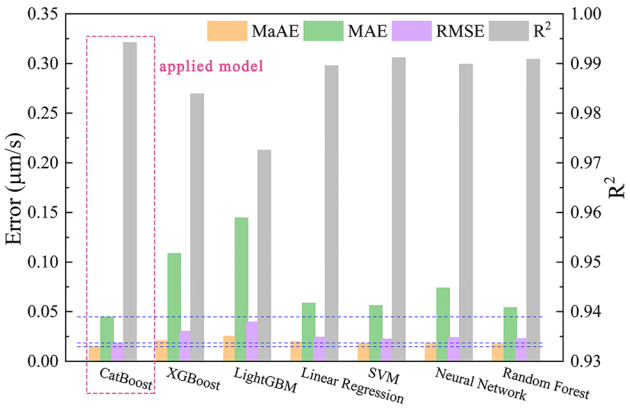

Fig. 18 Comparison of prediction results of different algorithms

5 Conclusions

This paper developed an MRR prediction model for robotic belt grinding of Inconel 718 based on abrasive belt images and the CatBoost algorithm, which had been validated with the experimental data. Based on the relevant analyses and results, the following conclusions can be drawn:

(1) Grinding force and belt speed have a great impact on the MRR, leading to quite different MRR curves under various grinding parameters. As a result of the same wear styles during belt grinding, the trends of MRR curves are similar, with a rapid decrease at first, followed by a gradual and smooth decline.

(2) The abrasive grain areal ratio C_r, color moments, and texture information of abrasive belt images are successfully extracted. They provide a good assessment of belt wear and demonstrate a strong correlation with MRR after normalization.

(3) An MRR prediction model based on the abrasive belt image features and CatBoost algorithm is established. The MaAE, MAE, RMSE, and R^2 of the prediction model are 0.17 μm, 0.4 μm, 0.2 μm, and 99.42%, respectively. Compared with other prediction models, the established model is more reliable. In practical applications, if the initial and terminated MRRs, as well as images from a new and failed abrasive belt, are acquired, the MRR prediction model can be applied.

In spite of its good prediction result, the proposed method is a data-driven approach, and the prediction accuracy depends greatly on the quality and volume of the experimental data used. In the future, we will explore the physical meaning behind the relationship between grain wear mechanisms, belt image features, and MRR.

Author contribution Yuxiang Wang: investigation, methodology, coding, analyzing, and writing — original draft. Xiaokang Huang: methodology. Xukai Ren: writing — review and editing. Ze Chai: writing — review and editing. Xiaoqi Chen: conceptualization, funding acquisition, and writing — review and revision.

Funding Open Access funding enabled and organized by CAUL and its Member Institutions. This work was supported by Chengzhi Technology Limited, Ningbo, China (Grant number: 20H500000043).

Data availability The data that support the findings of this study are available from the corresponding author upon reasonable request.

Code availability All the code of this study is available from the corresponding author upon reasonable request.

Declarations

Ethics approval Not applicable.

Consent to participate The manuscript has been read and approved by all authors.

Consent for publication Not applicable.

Competing interests The authors declare no competing interests.

References

1. Wang YJ, Huang Y, Chen YX, Yang ZS (2016) Model of an abrasive belt grinding surface removal contour and its application. Int J Adv Manuf Technol 82:2113–2122. https://doi.org/10.1007/s00170-015-7484-5
2. Fan W, Wang W, Wang J et al (2021) Microscopic contact pressure and material removal modeling in rail grinding using abrasive belt. Proc Inst Mech Eng Part B J Eng Manuf 235:3–12. https://doi.org/10.1177/0954405420932419
3. Xiao GJ, Huang Y, Yang YH, Yi H (2014) Workpiece surface integrity of GH4169 nickel-based superalloy when employing abrasive belt grinding method. Adv Mater Res 936:1252–1257. https://doi.org/10.4028/www.scientific.net/AMR.936.1252
4. Klocke F, Linke B, Schluetter D (2010) Development of a reliable grinding procedure for ceramic medical instruments. Prod Eng 4:571–579. https://doi.org/10.1007/s11740-010-0257-y
5. Roth JT, Djurdjanovic D, Yang X et al (2010) Quality and inspection of machining operations: tool condition monitoring. J Manuf Sci Eng Trans ASME 132:0410151–04101516. https://doi.org/10.1115/1.4002022
6. Yan S, Xu X, Yang Z et al (2019) An improved robotic abrasive belt grinding force model considering the effects of cut-in and cut-off. J Manuf Process 37:496–508. https://doi.org/10.1016/j.jmapro.2018.12.029
7. Xu X, Chen W, Zhu D et al (2021) Hybrid active/passive force control strategy for grinding marks suppression and profile accuracy enhancement in robotic belt grinding of turbine blade. Robot Comput Integr Manuf 67:102047. https://doi.org/10.1016/j.rcim.2020.102047
8. Agrawal SS, Yadava V (2013) Modeling and prediction of material removal rate and surface roughness in surface-electrical discharge diamond grinding process of metal matrix composites. Mater Manuf Process 28:381–389. https://doi.org/10.1080/10426914.2013.763678
9. Chen Z, Shi Y, Lin X (2018) Evaluation and improvement of material removal rate with good surface quality in TC4 blisk blade polishing process. J Adv Mech Des Syst Manuf 12:1–12. https://doi.org/10.1299/jamdsm.2018jamdsm0083
10. Song J, Yao Y (2015) Material removal model considering influence of curvature radius in bonnet polishing convex surface. Chinese J Mech Eng (English Ed 28:1109–1116. https://doi.org/10.3901/CJME.2015.0923.114
11. Ho LT, Cheung CF, Blunt L, Zeng S (2015) An investigation of factors affecting and optimizing material removal rate in computer controlled ultra-precision polishing. Key Eng Mater 625:446–452. https://doi.org/10.4028/www.scientific.net/KEM.625.446
12. Li F, Xue Y, Zhang Z et al (2020) Optimization of grinding parameters for the workpiece surface and material removal rate in the belt grinding process for polishing and deburring of 45 steel. Appl Sci 10. https://doi.org/10.3390/APP10186314
13. Li L, Ren X, Feng H et al (2021) A novel material removal rate model based on single grain force for robotic belt grinding. J Manuf Process 68:1–12. https://doi.org/10.1016/j.jmapro.2021.05.029
14. Cheng C, Li J, Liu Y et al (2019) Deep convolutional neural network-based in-process tool condition monitoring in abrasive belt grinding. Comput Ind 106:1–13. https://doi.org/10.1016/j.compind.2018.12.002
15. Pandiyan V, Caesarendra W, Tjahjowidodo T, Tan HH (2018) In-process tool condition monitoring in compliant abrasive belt grinding process using support vector machine and genetic algorithm. J Manuf Process 31:199–213. https://doi.org/10.1016/j.jmapro.2017.11.014
16. Chen J, Chen H, Xu J et al (2018) Acoustic signal-based tool condition monitoring in belt grinding of nickel-based superalloys using RF classifier and MLR algorithm. Int J Adv Manuf Technol 98:859–872. https://doi.org/10.1007/s00170-018-2270-9
17. Qi J, Chen B, Zhang D (2020) Multi-information fusion-based belt condition monitoring in grinding process using the improved-Mahalanobis distance and convolutional neural networks. J Manuf Process 59:302–315. https://doi.org/10.1016/j.jmapro.2020.09.061
18. Chen X, Limchimchol T (2006) Monitoring grinding wheel redress-life using support vector machines. Int J Autom Comput 3:56–62. https://doi.org/10.1007/s11633-006-0056-2
19. Yang Z, Yu Z (2013) Experimental study of burn classification and prediction using indirect method in surface grinding of AISI 1045 steel. Int J Adv Manuf Technol 68:2439–2449. https://doi.org/10.1007/s00170-013-4882-4
20. Gao K, Chen H, Zhang X et al (2019) A novel material removal prediction method based on acoustic sensing and ensemble XGBoost learning algorithm for robotic belt grinding of Inconel 718. Int J Adv Manuf Technol 105:217–232. https://doi.org/10.1007/s00170-019-04170-7
21. Wang N, Zhang G, Ren L et al (2021) Vision and sound fusion-based material removal rate monitoring for abrasive belt grinding using improved LightGBM algorithm. J Manuf Process 66:281–292. https://doi.org/10.1016/j.jmapro.2021.04.014
22. Wang N, Zhang G, Ren L et al (2022) In-process material removal rate monitoring for abrasive belt grinding using multisensor fusion and 2D CNN algorithm. Int J Adv Manuf Technol. https://doi.org/10.1007/s00170-022-08768-2
23. Wang N, Zhang G, Pang W et al (2021) Novel monitoring method for material removal rate considering quantitative wear of abrasive belts based on LightGBM learning algorithm. Int J Adv Manuf Technol 114:3241–3253. https://doi.org/10.1007/s00170-021-06988-6
24. Dorogush AV, Ershov V, Gulin A (2018) CatBoost: gradient boosting with categorical features support. arXiv preprint arXiv:1810.11363
25. Singh SM, Hemachandran K (2012) Content-based image retrieval using color moment and Gabor texture feature. Int J Comput Sci Issues (IJCSI) 9(5):299
26. Zhu C, Yang X (1998) Study of remote sensing image texture analysis and classification using wavelet. Int J Remote Sens 19:3197–3203. https://doi.org/10.1080/014311698214262
27. Castellano G, Bonilha L, Li LM, Cendes F (2004) Texture analysis of medical images. Clin Radiol 59:1061–1069. https://doi.org/10.1016/j.crad.2004.07.008
28. Xiao L, Wang Y, Nanjing li gong da xue et al (2015) Proceedings of 2015 IEEE International Conference on Progress in Informatics and Computing: PIC 2015 : 18–20 Dec 2015, Nanjing, China
29. Medeiros FNS, Ramalho GLB, Bento MP, Medeiros LCL (2010) On the evaluation of texture and color features for nondestructive

corrosion detection. EURASIP J Adv Signal Process 2010. https://doi.org/10.1155/2010/817473
30. Bharati MH, Liu JJ, MacGregor JF (2004) Image texture analysis: Methods and comparisons. Chemom Intell Lab Syst 72:57–71. https://doi.org/10.1016/j.chemolab.2004.02.005
31. Prokhorenkova L, Gusev G, Vorobev A et al (2017) CatBoost: unbiased boosting with categorical features. Adv Neural Inf Process Syst 31
32. Hammann G (1998) Modellierung des Abtragsverhaltens elastischer, robotergeführter Schleifwerkzeuge. Model des Abtragsverhaltens elastischer, Robot Schleifwerkzeuge. https://doi.org/10.1007/978-3-662-08796-1
33. Merchant HD, Murty GS, Bahadur SN et al (1973) Hardness-temperature relationships in metals. J Mater Sci 8:437–442. https://doi.org/10.1007/BF00550166